1

Structural sensitivity of spiral vortex breakdown

UBAID ALI QADRI,
DHIREN MISTRY AND MATTHEW P. JUNIPER

Department of Engineering, University of Cambridge,
Trumpington Street, Cambridge, CB2 1PZ, U.K.

Previous numerical simulations have shown that vortex breakdown starts with the formation of a steady axisymmetric bubble and that an unsteady spiralling mode then develops on top of this. We investigate this spiral mode with a linear global stability analysis around the steady bubble and its wake. We obtain the linear direct and adjoint global modes of the linearized Navier–Stokes equations and overlap these to obtain the structural sensitivity of the spiral mode, which identifies the wavemaker region. We also identify regions of absolute instability with a local stability analysis. At moderate swirls, we find that the $m = -1$ azimuthal mode is the most unstable and that the wavemaker regions of the $m = -1$ mode lie around the bubble, which is absolutely unstable. The mode is most sensitive to feedback involving the radial and azimuthal components of momentum in the region just upstream of the bubble. To a lesser extent, the mode is also sensitive to feedback involving the axial component of momentum in regions of high shear around the bubble. At an intermediate swirl, in which the bubble and wake have similar absolute growth rates, other researchers have found that the wavemaker of the nonlinear global mode lies in the wake. We agree with their analysis but find that the regions around the bubble are more influential than the wake in determining the growth rate and frequency of the linear global mode. The results from this paper provide the first steps towards passive control strategies for spiral vortex breakdown.

1. Introduction

If a jet of fluid rotates with sufficient azimuthal velocity (swirl), a stagnation point and a recirculation bubble form within it, around one or two jet diameters downstream from the start of the jet. In this paper, the transition from the flow without a breakdown bubble to the flow with a breakdown bubble is labelled *axisymmetric* vortex breakdown. Furthermore, in some conditions the steady flow around this vortex breakdown bubble is unstable to helical perturbations. In this paper, the development of these helical perturbations on top of the vortex breakdown bubble is labelled *spiral* vortex breakdown.

Vortex breakdown was first observed in the flow over a gothic wing at high angles of attack by Peckham & Atkinson (1957). The spiral mode was first identified by Lambourne & Bryer (1961) in the flow over delta wings. Since then, several different forms of vortex breakdown have been observed in a variety of experimental settings such as tubes, nozzles and combustion chambers. Investigators often observed the axisymmetric and spiral modes of breakdown to occur almost simultaneously. Some saw spiral breakdown before axisymmetric breakdown, while others saw axisymmetric breakdown before spiral breakdown. This led to disagreements over the nature of vortex breakdown (see

reviews by Hall 1972; Leibovich 1978; Escudier 1988; Lucca-Negro & O'Doherty 2001).

Two main explanations have been proposed for vortex breakdown: hydrodynamic instability (Ludwieg 1960) and a supercritical to subcritical transition (Benjamin 1962). Experimental evidence reviewed by Escudier (1988) indicates that the flow upstream of the breakdown bubble is marginally stable or completely stable. Together with the fact that the onset of vortex breakdown is sudden, this suggests that hydrodynamic instability is not responsible for causing axisymmetric vortex breakdown. Benjamin (1962) compared vortex breakdown to the hydraulic jump seen in channel flows. He proposed the idea of vortex breakdown being a transition from a super-critical flow configuration to a sub-critical flow configuration and derived a criterion for vortex breakdown.

Numerical studies allow vortex breakdown to be studied in a more controlled manner. Grabowski & Berger (1976) observed axisymmetric breakdown bubbles in their steady incompressible simulations and tried, unsuccessfully, to apply Benjamin's criticality criterion to these flows. Over the next 20 years, increased computing power led to a large number of numerical studies in which vortex breakdown was simulated in a variety of domains (Spall & Snyder 1999). More recently, Ruith, Chen, Meiburg & Maxworthy (2003) carried out both steady axisymmetric and unsteady three-dimensional direct numerical simulations of vortex breakdown using the inlet flow profile defined by Grabowski & Berger (1976), which is labelled the *Grabowski* profile. They used constant inlet conditions and open lateral boundary conditions. They showed that Benjamin's criticality criterion works when applied locally to the flow profiles upstream of breakdown. Following this, Vyazmina, Nichols, Chomaz & Schmid (2009) studied the bifurcation sequence of axisymmetric vortex breakdown using the Grabowski inlet profile. Apart from noting that axisymmetric vortex breakdown is a robust transition phenomenon from one steady state to another, we do not investigate it further here.

Ruith *et al.* (2003) considered the local absolute/convective stability (Huerre & Monkewitz 1990) of the flow field created by the axisymmetric vortex breakdown. By comparing the flow profiles to those of a Batchelor vortex, they concluded that spiral breakdown is caused by a sufficiently large pocket of absolute instability in the wake of the axisymmetric breakdown bubble. They also obtained eigenfunctions corresponding to a helical (with azimuthal wavenumber $m = -1$) and double helical breakdown mode ($m = -2$). The minus sign indicates that the spiral winds in the opposite direction to the swirl.

Gallaire, Ruith, Meiburg, Chomaz & Huerre (2006) performed a local stability analysis of the flow fields obtained by Ruith *et al.* (2003) using linear direct numerical simulations (lDNS). For a particular swirl parameter, they found two regions of absolute instability, one centred on the bubble and one centred on the wake that develops behind it. By using the frequency selection criterion of Pier, Huerre & Chomaz (2001) and by comparing the spatial growth rate obtained from the local analysis with amplitudes extracted from Ruith's DNS results, they interpreted spiral vortex breakdown as a nonlinear global mode that arises from the region of absolute instability in the wake of the bubble. Meliga & Gallaire (2011) performed a linear global stability analysis around the vortex breakdown bubble and its wake. They confirmed that spiral vortex breakdown is caused by an unstable eigenmode. The growth rate and frequency from their global stability analysis agreed well with the growth rate seen in Ruith's DNS. Recently, these researchers have extended their analysis to consider weakly nonlinear mechanisms that are responsible for competition between the helical and double helical breakdown modes in the Grabowski

family of flows (Meliga, Gallaire & Chomaz 2012).

In this paper, we investigate spiral vortex breakdown in laminar, incompressible flows by performing linear global stability analyses around the vortex breakdown bubble and its wake. In contrast to Meliga & Gallaire (2011) and Meliga *et al.* (2012), our aim is to determine the regions that are most influential in causing spiral breakdown as observed in the simulations of Ruith *et al.* (2003) and to identify the physical mechanisms that are responsible for causing it.

For this purpose, we use the linear direct and adjoint global modes to obtain the structural sensitivity of the flow (Hill 1992; Giannetti & Luchini 2007). This provides a two-dimensional map of the wavemaker region of the flow, showing the regions of the flow in which force-momentum feedback has most influence on the frequency and growth rate of the mode. We also perform a local stability analysis, which allows us to work out which regions of the flow are absolutely unstable and extract local spatial growth rates of perturbations, given the frequency of the global mode. This is a useful diagnostic tool, particularly in identifying the wavefront of the nonlinear global mode. We compare our results with those of Ruith *et al.* (2003) and Gallaire *et al.* (2006) and, although we agree with Gallaire *et al.* (2006) that the nonlinear behaviour is governed by the wake, we discover that the linear behaviour is governed by the bubble for moderate swirls.

This study is at $Re = 200$ and the primary motivation is scientific. There are important industrial motivations, however. Vortex breakdown occurs in wingtip vortices behind aircraft, in vacuum cleaners, and in gas turbine combustion chambers. In the case of combustion chambers, hydrodynamic instabilities in the flow can lock into acoustic resonances within the combustion chamber, causing high amplitude thermoacoustic instabilities, which can be catastropic. This fundamental study of spiral vortex breakdown will reveal the regions of the flow that are responsible for these hydrodynamic instabilities and could help designers to control them, either actively or passively.

2. Methodology

First we calculate a steady base flow using the nonlinear Navier–Stokes equations. Then we consider infinitesimal perturbations to this base flow and use a global stability analysis to calculate the direct linear global modes that would grow or decay on this base flow. We also calculate the corresponding adjoint global modes, which can be overlapped with the direct global modes in order to reveal the wavemaker region of the flow. Finally, we perform a local stability analysis on the base flow. The two-dimensional global modes have already been calculated with the global analysis so we use the local analysis as a diagnostic tool, rather than as a predictive tool. This reveals the regions of the flow that are absolutely unstable and adds physical insight to the results of the global analysis.

2.1. *The domain and the governing equations*

We study the motion of a viscous fluid in a cylindrical domain with length X_{max} and radius R_{max}, using cylindrical coordinates (x, r, θ). The flow has density ρ, pressure p, temperature T, and velocity $\mathbf{u} = (u_x, u_r, u_\theta)^T$. The inlet boundary, at $x = 0$, is labelled Ω_{in}. The outlet boundary, at $x = X_{max}$, is labelled Ω_{out}. The lateral boundary, at $r = R_{max}$, is labelled Ω_{lat}.

Non-dimensional variable	Definition	Non-dimensional parameter	Definition
Length	$x \equiv \frac{x^*}{R}$	Mach number	$Ma \equiv \frac{U_1}{\gamma R_g T_1}$
Velocity	$\mathbf{u} \equiv \frac{\mathbf{u}^*}{U_1}$	Density ratio	$S_1 \equiv \frac{\rho_1}{\rho_1} = 1$
Temperature	$T \equiv \frac{T^* - T_0}{T_1 - T_0}$	Reynolds number	$Re \equiv \frac{\rho_1 U_1 R}{\mu}$
Pressure, p	$p \equiv \frac{p^*}{\rho_1 R_g T_1}$	Prandtl number	$Pr \equiv \frac{\mu c_p}{\lambda}$
Density	$\rho \equiv \frac{\rho^*}{\rho_1}$	Richardson number	$Ri \equiv \frac{gR}{U_1^2}$
Time	$t \equiv \frac{t^* U_1}{R}$		

TABLE 1. Non-dimensional variables and parameters defined in terms of dimensional variables (starred), physical constants (where R_g is the gas constant, c_p is the specific heat capacity at constant pressure, γ is the ratio of specific heats, μ is the dynamic viscosity, λ is the thermal conductivity, and g is the acceleration due to gravity) and the entry conditions (§3.1).

We use a low Mach number (LMN) formulation of the Navier–Stokes equations because the code has already been validated (Nichols, Schmid & Riley 2007; Chandler, Juniper, Nichols & Schmid 2012) and because we will consider flows with non-uniform temperature and composition next. In this paper, the density is uniform and the incompressible Navier–Stokes equations could have been used. In non-dimensional form, the LMN equations are

$$\frac{\partial \rho}{\partial t} + \nabla \cdot (\rho \mathbf{u}) = 0 \qquad (2.1a)$$

$$\frac{\partial(\rho \mathbf{u})}{\partial t} = -\nabla p + \nabla \cdot (\frac{1}{S_1 Re}\tau - \rho \mathbf{u}\mathbf{u}) + Ri(1 - \rho)\hat{\mathbf{g}}, \qquad (2.1b)$$

$$\rho(\frac{\partial T}{\partial t} + \mathbf{u} \cdot \nabla T) = \frac{1}{S_1 Re Pr}\nabla^2 T, \qquad (2.1c)$$

$$\rho\left[(S_1 - 1)T + 1\right] = 1, \qquad (2.1d)$$

where $\tau = \left[\nabla \mathbf{u} + (\nabla \mathbf{u})^T\right] - \frac{2}{3}(\nabla \cdot \mathbf{u})I$ is the viscous stress tensor. The other non-dimensional variables and parameters are defined in table 1. The species equation has the same form as the temperature equation but is not used here and is omitted for brevity. In the uniform density case, $\rho = 1$, $T = 0$ and $S_1 = 1$ and the equations above reduce to the incompressible Navier–Stokes equations.

2.2. *The direct and adjoint perturbation equations*

We obtain a steady solution to (2.1) using the procedure described in §3.1, and it is labelled $\bar{\mathbf{u}}, \bar{\rho}$ *etc.* The evolution of small perturbations, which are labelled $\mathbf{u}', \rho'$ *etc.*, on top of the base flow is governed by the linearized equations of motion:

$$\frac{\partial \rho'}{\partial t} = -\nabla \cdot \mathbf{m}', \qquad (2.2a)$$

$$\frac{\partial \mathbf{m}'}{\partial t} = -\nabla p - \nabla \cdot (\bar{\rho}\bar{\mathbf{u}}\mathbf{u}' + \bar{\rho}\mathbf{u}'\bar{\mathbf{u}} + \rho'\bar{\mathbf{u}}\bar{\mathbf{u}}) + \frac{1}{S_1 Re}\nabla \cdot \tau' + Ri\rho'\hat{\mathbf{g}}, \qquad (2.2b)$$

$$\bar{\rho}\frac{\partial T'}{\partial t} = -\mathbf{m}' \cdot \nabla \bar{T} - \bar{\rho}\bar{\mathbf{u}} \cdot \nabla T' + \frac{1}{S_1 Re Pr}\nabla^2 T', \qquad (2.2c)$$

$$\frac{\rho'}{\bar{\rho}} = -\frac{(S_1 - 1)T'}{((S_1 - 1)\bar{T} + 1)}, \tag{2.2d}$$

where $\mathbf{m}' \equiv \bar{\rho}\mathbf{u}' + \rho'\bar{\mathbf{u}}$ is the linearized momentum and $\tau' = \left[\nabla\mathbf{u}' + (\nabla\mathbf{u}')^T\right] - \frac{2}{3}(\nabla \cdot \mathbf{u}')I$ is the linearized viscous stress tensor. This set of equations can be represented as

$$\frac{d\mathbf{q}}{dt} = \mathbf{L}\mathbf{q}, \tag{2.3}$$

where $\mathbf{q} \equiv (m'_x, m'_r, m'_\theta, T', p')^T$ is the state vector and $\mathbf{L}$ represents the Navier–Stokes equations linearized about the base flow. The density ρ' is not included in the state vector because it can derived from the temperature T' by using (2.2d).

These linear perturbations can be decomposed into Fourier modes in time and the azimuthal direction:

$$\mathbf{q}(x, r, \theta, t) = \hat{\mathbf{q}}(x, r)e^{\mathrm{i}m\theta + \lambda t}, \tag{2.4}$$

where m is the azimuthal wavenumber and $\lambda \equiv \sigma + \mathrm{i}\omega$ contains the growth rate, σ, and frequency, ω. We study the linear dynamics of the flow by analyzing the eigenvalues of $\mathbf{L}$. These are obtained by solving the matrix eigenvalue problem

$$\lambda\hat{\mathbf{q}} = \mathbf{L}_m\hat{\mathbf{q}}, \tag{2.5}$$

where $\mathbf{L}_m$ is the linear operator for the azimuthal wavenumber m (Appendix A.1). Each of these eigenvalues has a corresponding two-dimensional eigenfunction, $\hat{\mathbf{q}}(x, r)$. We label each eigenvalue/eigenfunction pair a *direct global mode*. If $\sigma > 0$, the mode is linearly globally unstable. In this linear analysis, the flow tends to the form of the global mode with highest σ in the long-time limit and therefore this mode determines the system's overall stability.

We now define an inner product over a volume, V,

$$\langle \mathbf{a}, \mathbf{b} \rangle = \frac{1}{V} \int_V \mathbf{a}^H \mathbf{b}\, dV, \tag{2.6}$$

where $\mathbf{a}^H$ denotes the Hermitian (*i.e.* complex conjugate transpose) of $\mathbf{a}$. The linear operator, $\mathbf{L}_m$, has a corresponding adjoint operator $\mathbf{L}_m^+$, which is defined in terms of an inner product:

$$\langle \hat{\mathbf{q}}^+, \mathbf{L}_m\hat{\mathbf{q}} \rangle \equiv \langle \mathbf{L}_m^+\hat{\mathbf{q}}^+, \hat{\mathbf{q}} \rangle. \tag{2.7}$$

This definition is valid for any pair of vectors, but it is convenient to express (2.7) in terms of the direct state vector, $\hat{\mathbf{q}}$, and the adjoint state vector, $\hat{\mathbf{q}}^+$.

The adjoint operator is derived from the direct governing equations by integration by parts. Chandler *et al.* (2012) found that the direct equations need to be rearranged into a suitable form before deriving the adjoint equations. This is necessary so that the two sets of equations can be solved using a similar algorithm, which reduces numerical errors that arise when solving the adjoint equations. The following set of adjoint LMN equations were found to be the most similar to the direct LMN equations

$$\frac{\partial m_i^+}{\partial x_i} = 0 \tag{2.8a}$$

$$-\frac{\partial m_i^+}{\partial t} = \frac{\bar{m}_j}{\bar{\rho}}\left(\frac{\partial m_i^+}{\partial x_j} + \frac{\partial m_j^+}{\partial x_i}\right) + \frac{1}{\bar{\rho}}\frac{\partial p^+}{\partial x_i} + \frac{1}{S_1 Re\bar{\rho}}\left(\frac{\partial^2 m_i^+}{\partial x_j^2} + \frac{1}{3}\frac{\partial^2 m_j^+}{\partial x_j \partial x_i}\right)$$

$$-\frac{T^+}{\bar{\rho}}\frac{\partial \bar{T}}{\partial x_i} \tag{2.8b}$$

$$-\frac{\partial T^+}{\partial t} = \bar{m}_i \frac{\partial}{\partial x_i}\left(\frac{T^+}{\bar{\rho}} + (S_1-1)p^+\right) + \frac{1}{S_1 RePr}\frac{\partial^2}{\partial x_i^2}\left(\frac{T^+}{\bar{\rho}} + (S_1-1)p^+\right)$$
$$- (S_1-1)\rho^+ \tag{2.8c}$$

$$\rho^+ = -\bar{m}_i \bar{m}_j \frac{\partial m_i^+}{\partial x_j} - Ri\bar{\rho}^2 m_i^+ g_i - \frac{\bar{m}_i}{S_1 Re}\left(\frac{\partial^2 m_i^+}{\partial x_j^2} + \frac{1}{3}\frac{\partial^2 m_j^+}{\partial x_j \partial x_i}\right) \tag{2.8d}$$

These can be written in the same form as for the direct equations:

$$-\frac{\mathrm{d}\mathbf{q}^+}{\mathrm{d}t} = \mathbf{L}^+ \mathbf{q}^+ \tag{2.9a}$$

$$\mathbf{q}^+(x,r,\theta,t) = \hat{\mathbf{q}}^+(x,r)e^{\mathrm{i}m\theta - \lambda^* t} \tag{2.9b}$$

$$\lambda^* \hat{\mathbf{q}}^+ = \tilde{\mathbf{L}}_m^+ \hat{\mathbf{q}}^+ \tag{2.9c}$$

where $\lambda^* \equiv \sigma - \mathrm{i}\omega$ is the complex conjugate of the corresponding direct eigenvalue. The adjoint global modes are then given by the solution of the eigenvalue problem in $(2.9c)$ (see Appendix A.2).

2.3. *The structural sensitivity*

The structural sensitivity, as developed by Hill (1992) and Giannetti & Luchini (2007), is given by the dyadic product of the direct and adjoint momentum vectors, $S_{ij} = \hat{\mathbf{m}}_i(\hat{\mathbf{m}}_j^+)^*$. The components of this complex-valued 3×3 tensor show how feedback between the components of the linearized momentum vector affects the growth rate and frequency of the global mode. Giannetti & Luchini (2007) used the Frobenius norm of the sensitivity tensor to identify where a modification in the linearized equations produces the greatest drift of the eigenvalue and thereby reveal the region of the flow that acts as the wavemaker. In our case, this is equivalent to evaluating the expression

$$|\nabla_G \lambda|_{max} = \frac{\|(\hat{\mathbf{m}}^+)^H\|\|\hat{\mathbf{m}}\|}{\langle \hat{\mathbf{m}}^+, \hat{\mathbf{m}} \rangle}, \tag{2.10}$$

where $\|\hat{\mathbf{m}}\|$ and $\|\hat{\mathbf{m}}^+\|$ represent the l^2-norm of the direct and adjoint global momentum vectors at each point in space. (Chandler *et al.* 2012).

2.4. *The local stability analysis*

The local analysis is performed using the technique described in Juniper, Tammisola & Lundell (2011). As for the global analysis, the velocity and pressure fields are decomposed into a steady base flow and a small perturbation. For the local analysis, we assume that the flow exhibits two well-separated length scales: an instability wavelength, λ_l, and a length scale that characterizes the stream-wise non-uniformity of the base flow, L_l. The ratio λ_l/L_l, which must be small for a local analysis to be rigorously valid, is labelled ϵ. In the flows examined in this paper, ϵ is small in the downstream region but large in the upstream region. This means that the local analysis becomes invalid in the upstream region, and we find that it cannot predict the global mode frequency and shape, as described in Juniper *et al.* (2011). Hence, we only use it to obtain the absolute growth rate at each streamwise location.

3. Numerical implementation

3.1. *Base flow*

The nonlinear governing equations (2.1) are solved by direct numerical simulation (DNS) with a modification of the code developed by Nichols *et al.* (2007). The equations are discretized on a collocated grid with S_x and S_r points in the axial and radial directions. Sixth-order compact finite difference schemes are used to calculate spatial derivatives in the axial and radial directions. A spectral decomposition is used in the azimuthal direction. The co-ordinate singularity at $r = 0$ (the centreline) is treated using an asymptotic method proposed by Constantinescu & Lele (2002). The equations are solved using an explicit pressure projection method and time-stepping is implemented through a fourth-order Runge-Kutta scheme. The coupling between the pressure and the momentum boundary conditions, however, restricts the code to being first order accurate in time. Full details of the code and the nonlinear solution algorithm can be found in Nichols *et al.* (2007).

On Ω_{in}, we impose the density and velocity profiles used by Grabowski & Berger (1976) and subsequently by Ruith *et al.* (2003). This Grabowski profile has uniform density, ρ_1, uniform temperature, T_1, and uniform axial velocity, U_1, beyond a characteristic radius R. Using these quantities as reference scales (table 1), the non-dimensional base flow inlet profile is

$$\bar{\rho}(0, r) = 1, \tag{3.1a}$$

$$\bar{T}(0, r) = 0, \tag{3.1b}$$

$$\bar{u}_x(0, 0 \leq r \leq 1) = \alpha + (1 - \alpha)\left(6 - 8r + 3r^2\right)r^2, \tag{3.1c}$$

$$\bar{u}_x(0, r > 1) = 1, \tag{3.1d}$$

$$\bar{u}_r(0, r) = 0, \tag{3.1e}$$

$$\bar{u}_\theta(0, 0 \leq r \leq 1) = r\left(2 - r^2\right)Sw, \tag{3.1f}$$

$$\bar{u}_\theta(0, r > 1) = Sw/r, \tag{3.1g}$$

where Sw is a non-dimensional swirl parameter and α is a non-dimensional co-flow parameter. In this study, which is at $Re = 200$, we keep $\alpha = 1$, which corresponds to a uniform axial velocity. In the past, the use of constant inlet conditions for simulating vortex breakdown has been criticised. However, Ruith *et al.* (2003) showed that this is a safe assumption as long as the inlet is super-critical, which is true for all the inlet profiles that we consider.

On the lateral and outlet boundaries, we impose boundary conditions that model flow into a semi-infinite domain in the downstream and radial directions. For the momentum, we set a traction-free boundary condition on Ω_{lat} ($\tau \cdot \hat{\mathbf{n}} = 0$ where $\hat{\mathbf{n}}$ is the unit vector normal to the boundary) and a convective boundary condition on Ω_{out} ($\partial\mathbf{m}/\partial t + U_c \cdot \partial\mathbf{m}/\partial x = 0$ with U_c set to the maximum outlet axial velocity). For the temperature, we use a homogeneous dirichlet condition ($T = 0$) on all boundaries. For the pressure, we set $p = 0$ on Ω_{lat} and $\partial p/\partial x = 0$ on Ω_{in} and Ω_{out}.

The steady axisymmetric base flow, satisfying equations (2.1) in the limit $\partial/\partial t \rightarrow 0$, is obtained by marching the equations forward in time, while constraining the flow variables to be axisymmetric at each timestep. This works because the base flow is stable to axisymmetric perturbations.

3.2. *Global stability analysis*

We solve the discretized version of the eigenvalue problems (2.5) and (2.9c) using ARPACK, a software library that implements the implicitly restarted Arnoldi algorithm (IRAM) (Lehoucq, Sorensen & Yang 1998) in order to obtain the eigenvalues and eigenfunctions of a standard eigenvalue problem. We obtain the matrix-vector products required by ARPACK using a timestepping approach. Following Heaton, Nichols & Schmid (2009), we use complex versions of the linear direct and adjoint codes developed by Chandler *et al.* (2012). Complex numbers are required in order to handle the imaginary components that arise when non-zero azimuthal modes of swirling flows are considered.

For the direct global mode, we use a homogeneous Dirichlet condition on Ω_{in} and Ω_{lat} and a convective boundary condition on Ω_{out} for the momentum and temperature. The boundary conditions for the adjoint have to be chosen such that the boundary terms arising from the derivation of the adjoint equations (2.8) are zero. It is sufficient to use homogeneous Dirichlet boundary conditions for the adjoint momentum and temperature on all boundaries. The boundary conditions for the pressure in the linear direct and adjoint codes are identical to those for the base flow. In this paper, we normalize the direct and adjoint global modes so that $\langle \hat{\mathbf{m}}, \hat{\mathbf{m}} \rangle = \langle \hat{\mathbf{m}}^{+}, \hat{\mathbf{m}}^{+} \rangle = 1$.

3.3. *Local stability analysis*

The numerical procedure is identical to that in Juniper *et al.* (2011). At each streamwise location, the governing equations arising from §2.4 are discretized on a Chebyshev-spaced grid in the r-direction. This produces a generalized matrix eigenvalue problem, which represents the dispersion relation for this slice of the flow. In this paper, 48 Chebyshev-spaced points are used between the centreline and top wall, which is sufficient that the eigenvalues change by $\sim 10^{-4}$ when the resolution is increased. We calculate the complex absolute frequency, ω_0, as a function of streamwise distance, x, by finding saddle points in the complex k-plane and then checking that they are valid pinch points, as defined by Briggs-Bers. The procedure is described in detail in Juniper *et al.* (2011).

4. Results

In this section, we begin by establishing the accuracy and reliability of our numerical procedures for a case with swirl parameter $Sw = 1.0$ at $Re = 200$ by comparing our results with those from previous studies. We then present the direct and adjoint eigenmodes at the point where the flow is just globally unstable and map out the regions that are most sensitive to external forcing and internal feedback. We use the structural sensitivity tensor to identify the physical mechanisms that determine the global behaviour of the flow. Finally, we return to consider the case with $Sw = 1.0$ in light of the previous sensitivity analysis.

4.1. *Validation*

Figure 1 shows the steady base flow at $Sw = 1.0$. There is an axisymmetric breakdown bubble around $x = 2$, which creates a wake downstream. The streamline pattern and the size and location of the bubble match that obtained in previous axisymmetric simulations (Grabowski & Berger 1976; Ruith *et al.* 2003; Meliga & Gallaire 2011). For this reference case, we calculate the base flow and linear global stability on three different meshes in order to assess the reliability and convergence of the results. The linear global stability analysis predicts one unstable eigenmode for $m = -1$ and no unstable eigenmodes
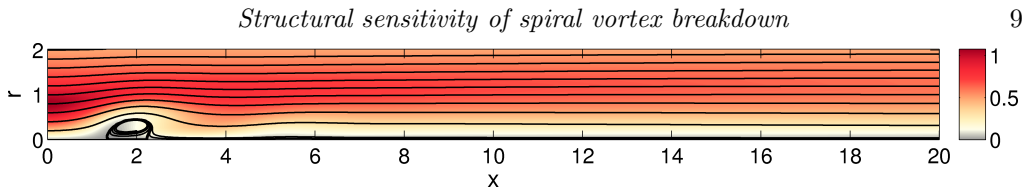
FIGURE 1. Non-dimensional base flow for $Sw = 1.0$, calculated with mesh M_1. The streamlines represent the axial and radial velocities. The shading (colour online) represents the azimuthal velocity.

	X_{max}	R_{max}	S_x	S_r	Growth rate σ	Frequency ω
M_1	20.0	8.0	513	127	0.035214	1.165476
M_2	20.0	8.0	257	127	0.035177	1.165453
M_3	25.4	10.4	257	127	0.034348	1.162470
Nonlinear DNS (Ruith *et al.* 2003)	20.0	10.0	193	61	0.0359	1.18
Local nonlinear analysis (Gallaire *et al.* 2006)	-	-	-	-	-	1.22
Linear global stability (Meliga & Gallaire 2011)	40.0	6.0	-	-	0.0335	1.17

TABLE 2. Domain size (X_{max}, R_{max}) and number of gridpoints (S_x, S_r) of the three meshes ($M_1 - M_3$) used in this study, and those used by Ruith *et al.* (2003) and Gallaire *et al.* (2006). Growth rate, σ, and frequency, ω, of the unstable mode in each study.

for $m \neq -1$. Table 2 compares the unstable global mode frequency obtained using these meshes with results from Ruith *et al.* (2003), Gallaire *et al.* (2006) and Meliga & Gallaire (2011). The eigenvalue depends very weakly on the grid resolution and spatial domain size and we conclude that mesh M_1 is sufficient for this study.

Ruith *et al.* (2003) performed fully three-dimensional nonlinear DNS. They perturbed the axisymmetric steady state solution with white noise and then extracted the linear growth rate and frequency from the initial rate of increase of the kinetic energy per unit mass. Our eigenvalue is within 1.3% of theirs. Gallaire *et al.* (2006) carried out a local stability analysis on the same axisymmetric steady state solution and used the frequency selection criterion of Pier *et al.* (2001) to predict the frequency of the nonlinear global mode. This is not expected to be exactly the same as the linear global mode but, nonetheless, is also close to our calculations. Meliga & Gallaire (2011) used a finite-element solver to obtain the base flow and global mode in a domain that was twice as long (axially) as that used in this study and by Ruith *et al.* (2003). As the domain length increases, the convective non-normality of the linearized N–S operator also increases. This makes the eigenvalues more sensitive to perturbations and this could be the reason for the slight discrepancy between our results and theirs.

Table 3 compares the linear growth rates obtained from mesh M_1 with those in Table 1 of Meliga & Gallaire (2011) and those in figure 28 of Ruith *et al.* (2003), for three swirls and two azimuthal wavenumbers, m. As discussed earlier, the difference between Meliga's growth rates and ours can be attributed to the difference in domain lengths. Ruith *et al.*'s extraction of the linear growth rate from the rate of growth of white noise works well near the point of linear stability, which is at $Sw = 0.915$, because only the $m = -1$ mode is unstable and this mode grows relatively slowly. It becomes less accurate as the swirl increases, however, because the $m = -2$ mode also becomes unstable. The evolution therefore depends on how the initial white noise projects onto each of the

Swirl	1.0	1.2	1.2	1.3	1.3
m	-1	-1	-2	-1	-2
σ from M_1	0.0352	0.114	0.0249	0.123	0.0693
σ from Ruith *et al.*	0.0359	0.106	0.0331	0.110	0.0674
σ from Meliga & Gallaire	0.0335	0.118	0.0264	0.125	0.0729

TABLE 3. Comparison of most unstable linear growth rates from a global stability analysis with growth rates observed in 3D DNS. The growth rates have been obtained from figure 28 of Ruith *et al.* (2003) and Table 1 of Meliga & Gallaire (2011) .

	Growth rate σ	Frequency ω	Absolute discrepancy	Relative discrepancy (%)
M_1	0.037663	-1.165434	0.002449	0.210064
M_2	0.037048	-1.165592	0.001876	0.160908
M_3	0.038603	-1.161601	0.004343	0.373424

TABLE 4. The most unstable adjoint eigenvalue for $m = -1$ and the discrepancy with respect to the complex conjugate of the direct eigenvalue, for meshes $M_1 - M_3$. The discrepancy is $\text{abs}(\lambda_{adj} - \lambda_{dir}^*)$ where $\lambda \equiv \sigma + \text{i}\omega$.

modes and it is harder to distinguish between the growth rates of each individual mode. This could explain why Ruith *et al.*'s growth rates at $Sw = 1.2$ and $Sw = 1.3$ are slightly different to ours. We conclude that the agreement is as good as can be expected.

In the absence of truncation errors, the adjoint eigenvalues would be the complex conjugates of the direct eigenvalues. In this study, the adjoint equations are derived algebraically from the direct equations and then discretized, which means that the truncation errors of the adjoint algorithm differ from those of the direct algorithm. We must check, therefore, that the adjoint eigenvalues are close to the complex conjugate of the direct eigenvalues. Table 4 shows the adjoint eigenvalues and the discrepancy with the direct eigenvalues for the three meshes. This discrepancy is due to the first order time accuracy of the numerical scheme and decreases as the timestep decreases (Chandler *et al.* 2012). The discrepancy for mesh M_1 is 0.2%, which is sufficiently small for us to be confident that the adjoint eigenmodes are correct.

4.2. *Formation of a recirculation bubble and the onset of instability*

In this study, we increase the swirl from $Sw = 0.8$, which is stable and before the onset of vortex breakdown. At $Sw = 0.8944$, a stagnation point forms on the centreline, which is the first sign of an axisymmetric breakdown bubble; figure 2. This agrees with the results of Ruith *et al.* (2003). The complex absolute growth rate, $\omega_{0\text{i}}$, is obtained as a function of streamwise distance, x, using the local analysis. This reveals that a region of absolute instability (which also exists for lower values of swirl) is centred around the bubble. The flow is globally stable, however, for all azimuthal wavenumbers, showing that this region of absolute instability is not large enough or strong enough to cause a global instability.

As the swirl is increased, an unstable mode ($\sigma > 0$) first appears at $Sw = 0.915$ with $m = -1$. Figure 3 shows the base flow at this swirl together with the absolute growth rate, the unstable direct mode, the corresponding adjoint mode, and the structural sensitivity map. For the direct and adjoint modes, the upper frame shows contours of the positive
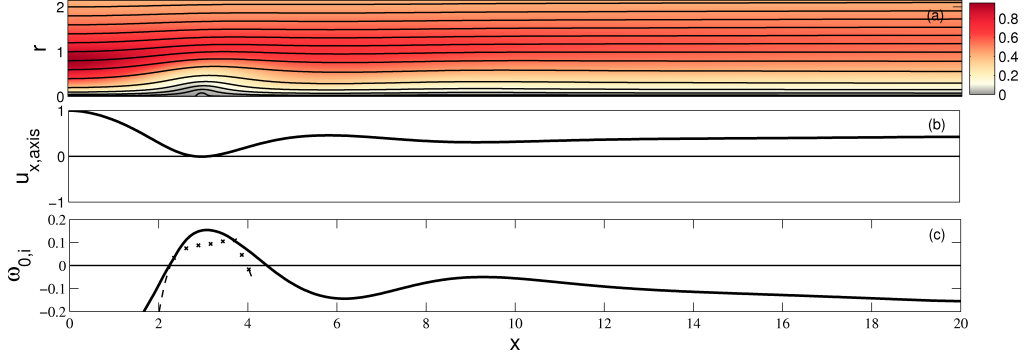
FIGURE 2. (a) Baseflow at $Sw = 0.8944$ and $Re = 200$, (b) axial velocity along the axis, $r = 0$, (c) absolute growth rate of the dominant saddle point (solid line) and the next saddle point (shown by a dashed line where it is a valid pinch point and by crosses where it is not).
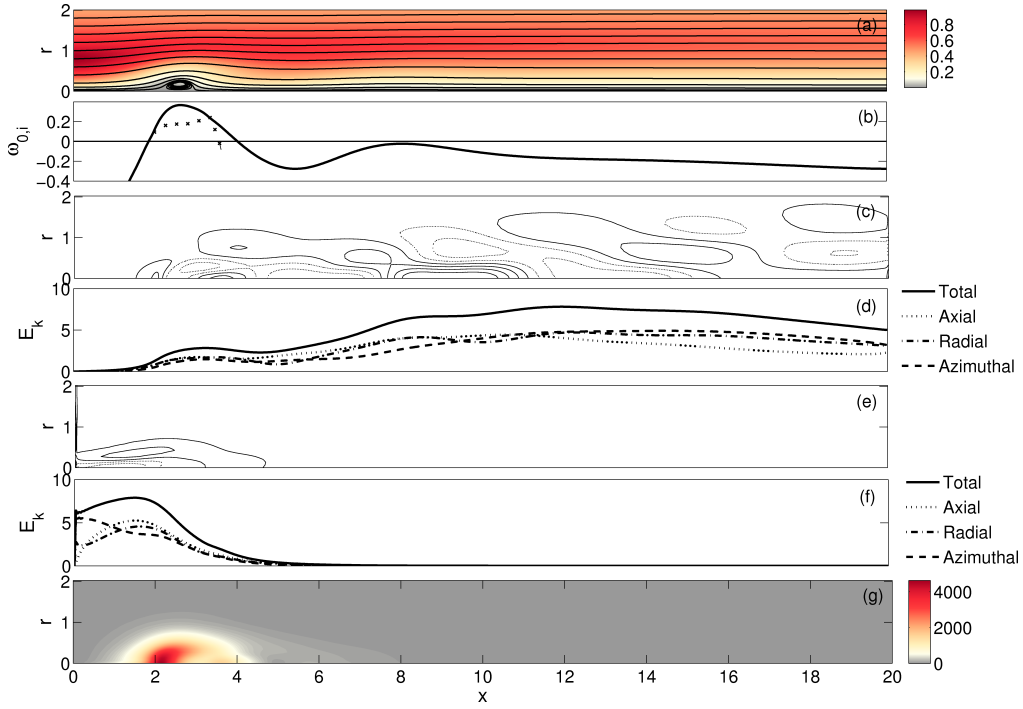

FIGURE 3. (a) Base flow at $Sw = 0.915$ and $Re = 200$; (b) absolute growth rate for $m = -1$; (c) azimuthal vorticity contours of the most unstable direct global mode (solid lines are positive values and dotted lines are negative values); (d) kinetic energy of this direct global mode, separated into the different velocity components; (e) azimuthal vorticity contours of the most unstable adjoint global mode; (f) kinetic energy of this adjoint global mode, separated into the different velocity components; (g) structural sensitivity map as defined by (2.10).

(solid) and negative (dotted) real parts of the azimuthal vorticity. (The imaginary parts have a similar structure but are a quarter wavelength out of phase.) The lower frame shows the kinetic energy, $E_k(x) = \int_0^{R_{max}} |\mathbf{u}|^2 r dr$ as a function of streamwise distance, and the contributions from the axial, radial, and azimuthal components. This is a convenient measure of the amplitude of the global mode.
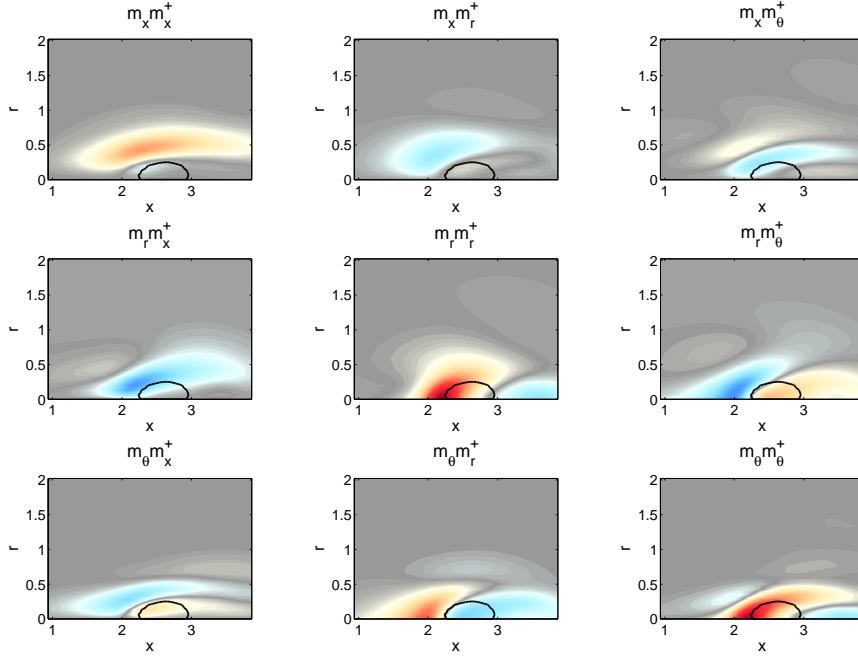
FIGURE 4. (Colour online) The real part (growth rate) of the components of the sensitivity tensor $S_{ij} = \hat{\mathbf{m}}_i (\hat{\mathbf{m}}_j^+)^*$ for the $m = -1$ mode at $Sw = 0.915$. The shading on all the plots scales from -2256 (blue) to 2256 (red). The thick black line shows the breakdown bubble.

At $Sw = 0.915$, the region of absolute instability around the breakdown bubble is sufficiently large to cause a global instability. The direct global mode starts to grow in the bubble region and is amplified further in the wake region, reaching a maximum around $x = 12$. It is worth noting that the wake region is convectively unstable, but not absolutely unstable. The adjoint global mode represents the receptivity of the direct mode to external forcing, or equivalently, the initial condition that most optimally excites the direct mode (Chomaz 2005). It is localized between the inlet and the upstream edge of the bubble. The spatial separation of the direct and adjoint global modes is characteristic of flows with convective non-normality (Chomaz 2005). For both the direct and adjoint global modes, the three velocity components have roughly the same order of magnitude, indicating that component-wise non-normality is not influential. If it were influential, one would expect different velocity components to dominate in the direct and adjoint global modes. The structural sensitivity map shows that the wavemaker region, as defined in (2.10), is located just upstream of the breakdown bubble, in the region of absolute instability.

4.2.1. Mechanisms of instability

In order to understand the physical mechanism by which a small perturbation to the linear operator affects the global mode, we consider the real and imaginary parts of the nine components of the structural sensitivity tensor, shown in Figures 4 and 5. The nine components quantify the sensitivity of the eigenvalue to changes in the feedback between the three components of the perturbation momentum vector and the three components of the linearized momentum equations. The real part describes the sensitivity of the growth rate, while the imaginary part describes the sensitivity of the frequency. For example,
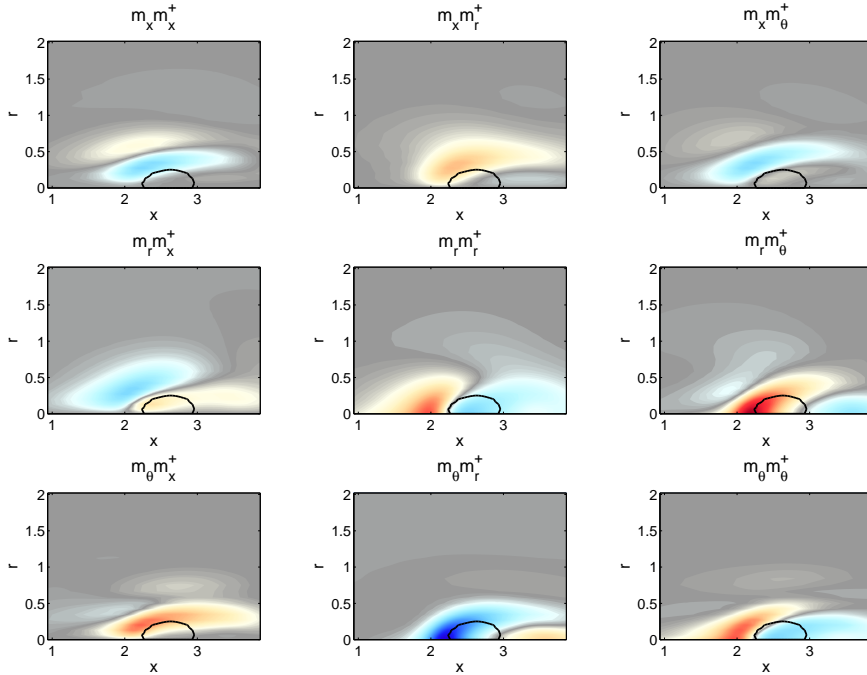
FIGURE 5. (Colour online) The imaginary part (frequency) of the components of the sensitivity tensor $S_{ij} = \hat{\mathbf{m}}_i(\hat{\mathbf{m}}_j^+)^*$ for the $m = -1$ mode at $Sw = 0.915$. The shading on all the plots scales from -2256 (blue) to 2256 (red). The thick black line shows the breakdown bubble.

the figure in the top right corner shows the effect of changing the amount of feedback from the streamwise momentum (m_x) to the azimuthal momentum equation (m_θ).

It can be seen that these sensitivities are in spatial quadrature: the imaginary component is large where the real component is zero, and vice-versa. These oscillatory sensitivity patterns are characteristic of convective flows and are caused by constructive or destructive interference (Tammisola 2012). The global mode arises due to contributions from feedback throughout the wavemaker region. These contributions interact constructively and destructively to give, in aggregate, a global mode frequency and growth rate. If the feedback at one point in this wavemaker region changes, then the effect on the global mode will depend on the amplitude and the phase of the feedback from this point, relative to the aggregate feedback from the other points. The phase relationship of the feedback varies in space, so the effect of a small change in the feedback at a point also varies in space.

The phase information is interesting, but a clearer picture of the influences of feedback between the components is given by the absolute value of the structural sensitivity. This is shown in figure 6. In order to understand the physical mechanisms that may be responsible for causing the global instability, it is worth comparing this with the nine components of the strain tensor of the base flow, $\epsilon_{ij} = \frac{1}{2}\left[\nabla\bar{\mathbf{u}} + (\nabla\bar{\mathbf{u}})^T\right]$, which are shown in figure 7. The three frames along the leading diagonal show the axial, radial and azimuthal strain, while the off-diagonal frames show the shear. We will start by considering four features. Firstly, at the entry plane, there is strong shear in the $r - \theta$ component at the edge of the vortex core. Secondly, just outside the edge of the bubble (at $r = 0.5$),
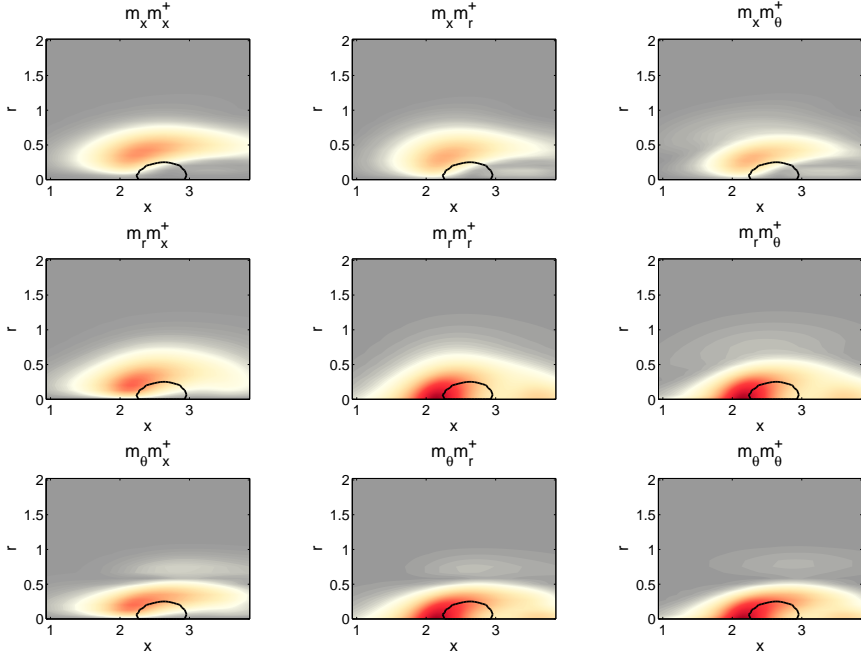
FIGURE 6. (Colour online) The absolute value of the components of the sensitivity tensor $S_{ij} = \hat{\mathbf{m}}_i(\hat{\mathbf{m}}_j^+)^*$ for the $m = -1$ mode of the flow at $Sw = 0.915$. The shading on all the plots scales from 0 (grey) to 2317 (red). The thick black line shows the breakdown bubble.
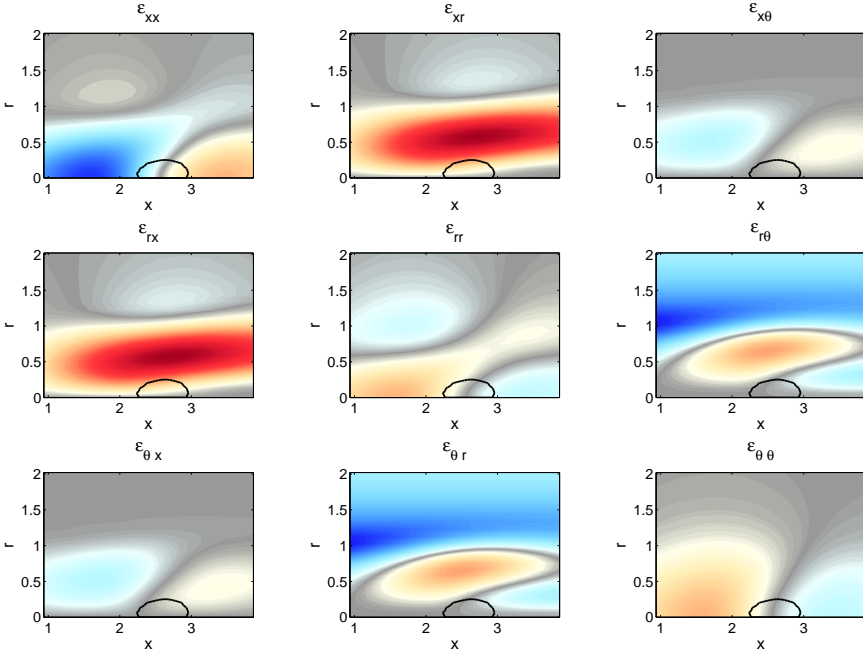

FIGURE 7. (Colour online) The components of the rate-of-strain tensor $\epsilon_{ij} = \frac{1}{2}\left[\nabla\bar{\mathbf{u}} + (\nabla\bar{\mathbf{u}})^T\right]$ for the base flow at $Sw = 0.915$. The shading on all the plots scales from -1.6 (blue) to 1.6 (red). The thick black line shows the breakdown bubble.
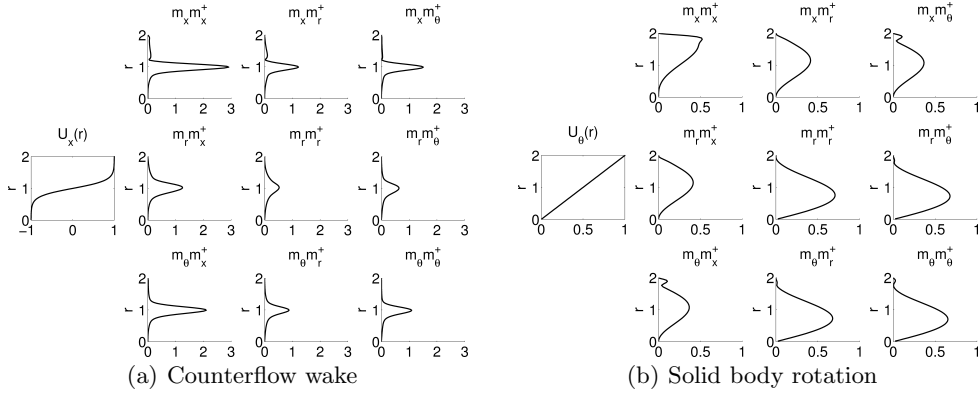
(a) Counterflow wake (b) Solid body rotation

FIGURE 8. The absolute value of the components of the sensitivity tensor $S_{ij} = \hat{\mathbf{m}}_i(\hat{\mathbf{m}}_j^+)^*$ for the $m = -1$ mode of (a) a parallel counterflow non-swirling wake, and (b) a vortex with solid body rotation. The single figures on the left in each subfigure show (a) the axial velocity profile of the wake base flow, and (b) the azimuthal velocity profile of the vortex base flow.

there is very strong shear in the $x - r$ component and weak shear in the $r - \theta$ component. Thirdly, the frames in the left column of figure 6, which correspond to the influences on the axial momentum equation, have high amplitudes in the region in which there is strong shear in the $x - r$ component. Fourthly, the frames in the top row of figure 6 , which correspond to the influence of the axial momentum, have moderate amplitudes in this region.

This can be compared with figure 8, which shows the nine components of the structural sensitivity tensor for the $m = -1$ mode in two parallel flows. The nine components have the same meaning that they have for the two-dimensional case in figures 4, 5 and 6: they quantify the sensitivity of the eigenvalue to changes in the feedback between the three components of the perturbation momentum vector and the three components of the perturbation momentum equations. The only differences are that the flow is parallel and that the perturbations are assumed to be of the form $\mathbf{u} \exp(\mathrm{i}kx)$ in the axial direction. This gives the local structural sensitivity. If the flow were non-parallel, this would be a cross-stream slice through the two-dimensional structural sensitivity.

The flow in figure 8(a) is a parallel non-swirling counterflow wake. This flow has uniform velocity in the axial direction and zero velocity in the radial and azimuthal directions. Therefore, all shear is concentrated in the $x - r$ component and only the Kelvin-Helmholtz (KH) mechanism is active. The frames in the left column of figure 8(a) have high amplitudes in the region in which there is strong shear in the $x - r$ component and the frames in the top row have moderate amplitudes in this region. It is also worth noting that the $r - r$ and $r - \theta$ components have low amplitudes. The centre-top frame of figure 7 shows that the $x - r$ component of shear is strong just outside the recirculation bubble (at $r = 0.5$). Figure 6 shows that the structural sensitivity is large in this region, particularly in the left column and top row. The comparison with figure 8(a) leads us to believe that the feedback in this region is caused by the KH mechanism.

The four bottom-right frames in figure 6 have high amplitudes around the upstream stagnation point of the recirculation bubble. From figure 7, we notice that this does not correspond to regions of large shear. Hence, this cannot be explained by a KH mechanism. To explain this, we consider the nine components of the sensitivity tensor for the

$m = -1$ mode in a flow with solid body rotation but no axial shear, shown in figure 8(b). For this flow, the highest sensitivities are in the $r - r$, $r - \theta$, $\theta - r$ and $\theta - \theta$ components, and they all have very similar magnitudes. This is typical of feedback that arises from the conservation of angular momentum. Specific examples of such a mechanism include the fictitious Coriolis force (Batchelor 1967, §7.6) and the generalized centrifugal instability mechanism proposed by Leibovich & Stewartson (1983), who derived a criterion for the temporal instability of a parallel Batchelor vortex in the limit of large azimuthal wavenumber, m, and large axial wavenumber, k. In these limits, the perturbation is only affected by the local flow. The perturbations in this paper, however, are far from the large m and k limit and are therefore not localized. Consequently, it is questionable whether they can be identified with the generalized centrifugal instability. Even if we ignore these concerns, we find, in this flow, that the criterion is only satisfied in regions of strong axial flow, where the perturbations have large group velocity. When deriving global properties from a local analysis, only the waves with zero group velocity contribute. On this basis, it seems unlikely that the generalized centrifugal instability is responsible for the strong feedback upstream of the breakdown bubble. We conclude simply that a mechanism involving conservation of angular momentum is active in the region just upstream of the breakdown bubble.

We can now explain why the adjoint global mode is large in the region upstream of the recirculation bubble, near the centreline (figure 3e). Let us consider the effect of a small open loop perturbation in this region. In this region, the axial vorticity of the base flow is an order of magnitude larger than the radial and azimuthal vorticity of the base flow. The perturbation vorticity is superposed on this. As a perturbation passes through this region, the fluid is compressed in the axial direction and stretched in the radial and azimuthal directions. By conservation of angular momentum, the vorticity in the radial and azimuthal directions increases, while the vorticity in the axial direction decreases. This increases the amplitude of the perturbation vorticity. The amplified perturbation then passes through the 'KH' region, where it is amplified by the classic Kelvin-Helmholtz mechanism. This description agrees with observations from experiments on vortex breakdown in swirling jets by Oberleithner, Sieber, Nayeri, Paschereit, Petz, Hege, Noack & Wygnanski (2011). These researchers found the wavemaker to be upstream of the breakdown bubble and the surrounding flow field to behave as an amplifier of upstream disturbances.

In summary, the nine components of the structural sensitivity reveal that, at the point of instability, two mechanisms are active in the wavemaker region of the global mode. The first is due to conservation of angular momentum in regions of strong strain in the flow, particularly upstream of the breakdown bubble. This mechanism is most sensitive to feedback involving the radial and azimuthal components of the perturbation momentum. The second is a classic KH mechanism in regions of strong shear. This mechanism is most sensitive to feedback involving the axial component of the perturbation momentum. We find that the first mechanism has more influence than the second on the growth rate and frequency of spiral vortex breakdown.

4.3. *Reference case, $Sw = 1.0$*

4.3.1. *Global stability analysis and structural sensitivity*

We now consider the reference case of $Sw = 1.0$ in light of the sensitivity analysis at $Sw = 0.915$. The main purpose of this section is to compare our linear global analysis with the nonlinear local analysis of Gallaire *et al.* (2006) and the weakly nonlinear global analysis of Meliga *et al.* (2012). Figure 9 presents the results of the stability analysis for
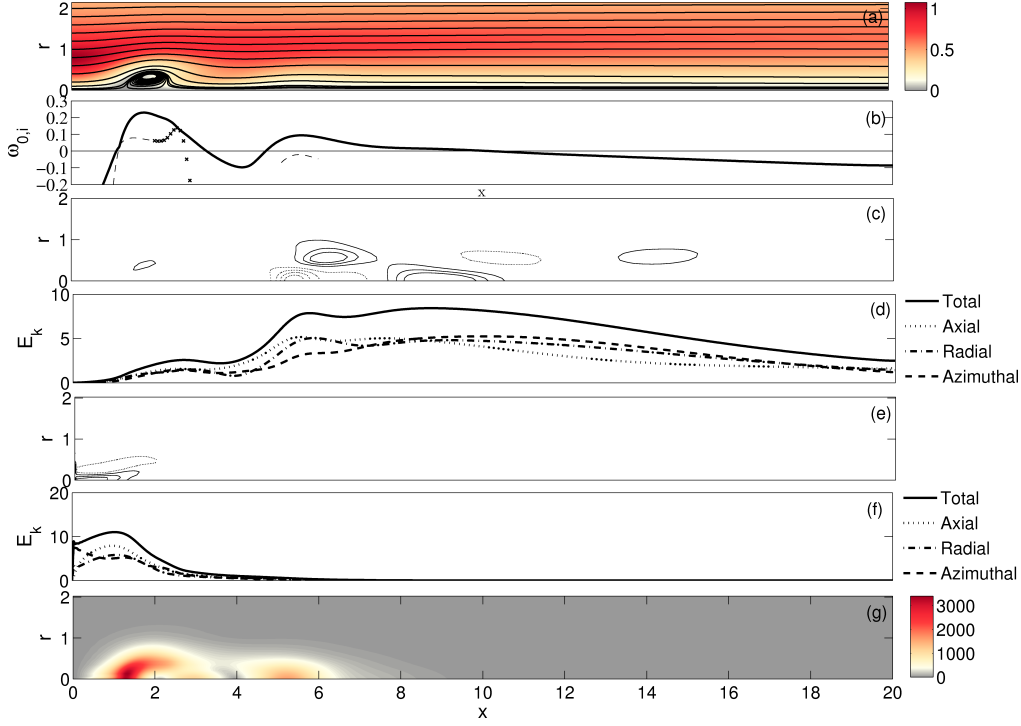
FIGURE 9. As for figure 3 but for $Sw = 1.0$. Frame (c) can be compared directly with Fig. 29(b) of Ruith *et al.* (2003) (but note that the vertical axis has been stretched in their figure)
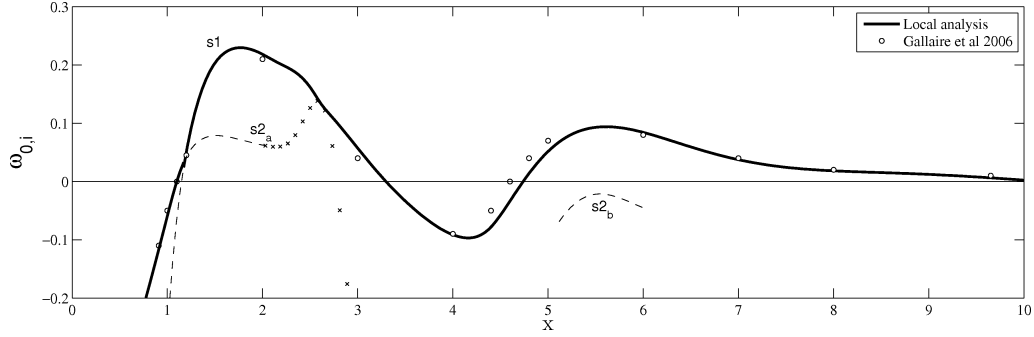

FIGURE 10. Local absolute growth rate, $\omega_{0,i}$, (thick line) as a function of streamwise distance for the $m = -1$ azimuthal wavenumber and $Sw = 1.0$. The thick line represents $\omega_{0,i}$ for the dominant saddle point ($s1$). The subdominant saddle points are shown by a dashed line where they are valid k^+/k^- pinch points and by crosses where they are not. The subdominant saddle points are located in regions of the flow in which there are two solutions of linear instability from the temporal analysis: the recirculation bubble (saddle $s2_a$) and the wake ($s2_b$). The streamwise domain of this flow extends to $x = 20$ but is not shown in this figure.

$Sw = 1.0$ in the same format as figure 3. The global mode shapes and spatial wavelengths agree very well with the DNS results in the linear regime shown in figure 29 of Ruith *et al.* (2003).

In agreement with Gallaire *et al.* (2006), figure 9(b) shows that the flow at $Sw = 1.0$ has two finite regions of absolute instability: a small region corresponding to the recircu-
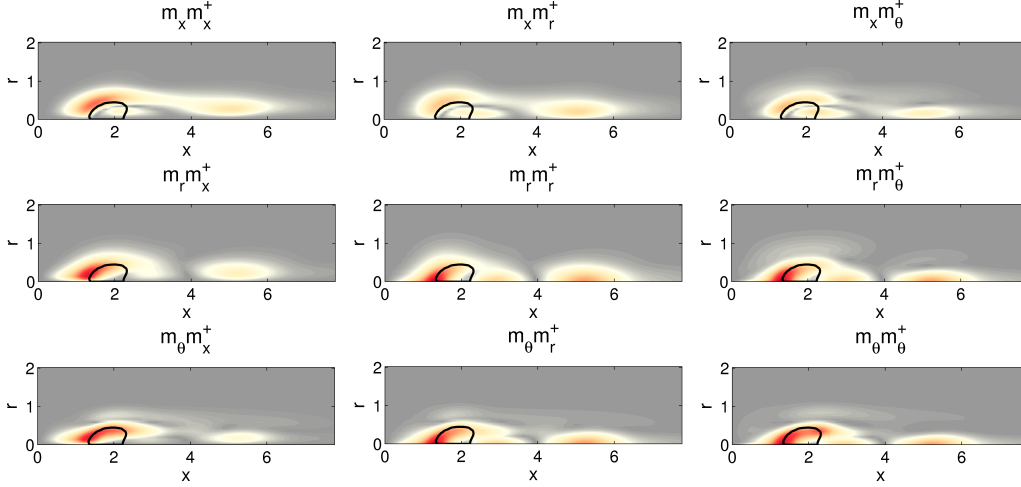
FIGURE 11. (Colour online) The absolute value of the components of the sensitivity tensor $S_{ij} = \hat{\mathbf{m}}_i(\hat{\mathbf{m}}_j^+)^*$ for the $m = -1$ mode at $Sw = 1.0$. The shading on all the plots scales from 0 (grey) to 1670 (red). The thick black line shows the breakdown bubble.

lation bubble and a large region corresponding to the wake. This is shown in more detail in figure 10, where our results are compared with results from figure 5 of Gallaire *et al.* (2006). Our results were obtained by locating saddle points of ω in the complex k-plane. Gallaire *et al.*'s results were obtained by extracting ω_{0i} from linear DNS of locally-parallel flows created from the actual flow at 15 streamwise locations. The results are in very good agreement with each other, even capturing saddle switching around $x = 1$.

The structural sensitivity map in figure 9(g) shows that there is a region of high sensitivity around the upstream end of the bubble, and regions of lower sensitivity downstream in the wake. In order to understand how each of these regions affects the global mode, we consider the components of the sensitivity tensor.

The real and imaginary parts (which are not shown here) are similar to figures 4 and 5 for $Sw = 0.915$ but show that the sensitive regions are not localised to just the bubble or just the wake in any component of the sensitivity tensor. This is evident in figure 11, which shows the absolute value of the sensitivity tensor at every point in the domain. In every plot, the regions around the bubble have greater sensitivity than the regions in the wake. Although both the bubble and the wake affect the instability, we deduce that the bubble is more influential than the wake in affecting both the growth rate and the frequency of the linear global mode.

4.3.2. *Comparison with nonlinear behaviour*

In contrast to the linear results, Gallaire *et al.* (2006) concluded that the nonlinear global behaviour is governed by the wake and not by the bubble. They extracted the spatial growth rate of perturbation kinetic energy from Ruith's saturated nonlinear DNS. They compared this with the spatial growth rates at the two points where the flow transitions from convective to absolute instability, in accordance with the nonlinear mode selection criterion of Pier *et al.* (2001). The spatial growth rate at the leading edge of the wake region matches that of the saddle point of the local analysis there. Our local

analysis gives the same results as that of Gallaire *et al.* (2006).

In summary, as the results in Table 2 show, the frequency predicted by the nonlinear local analysis in the wake is very close to the limit-cycle frequency measured in Ruith's DNS. The frequency predicted by our linear global analysis is also close to this limit-cycle frequency. However, our sensitivity analysis finds that the bubble is more influential than the wake in determining this frequency. We have not yet been able to find a convincing explanation for this behaviour. One possibility is to consider the nonlinear modification of the baseflow due to the direct global mode. This would be largest in the wake, close to where the direct global mode reaches a maximum. In our flow, the linear wavemaker region is quite far upstream of this location. For small steps beyond the bifurcation point (at $Sw = 0.915$), we would expect the flow to be significantly modified in the wake (Chomaz 2005), which Meliga *et al.* (2012) found to be the case.

5. Concluding remarks

In this paper, we have studied the linear global stability of the steady axisymmetric vortex breakdown bubble observed in the simulations of Ruith *et al.* (2003). We have confirmed that spiral vortex breakdown is caused by an unstable eigenmode of azimuthal wavenumber $m = -1$. The adjoint of this direct global mode has also been calculated. By overlapping the direct and the adjoint global modes, we have found the location of the wavemaker, which can be interpreted as the region responsible for causing spiral vortex breakdown (Giannetti & Luchini 2007). By considering the nine components of the structural sensitivity tensor, we have identified the physical mechansims that are responsible for causing spiral vortex breakdown. We have also used a local stability analysis to work out the regions of absolute instability in the flow.

When the $m = -1$ mode first goes unstable, at $Sw = 0.915$, the wavemaker is located just upstream of the breakdown bubble, which is the only region of the flow that is absolutely unstable. The structural sensitivity tensor reveals that this mode is caused by two physical mechanisms. The first mechanism is most sensitive to feedback between the radial and azimuthal components of the perturbation momentum, corresponding to the region of strong strain just upstream of the breakdown bubble. We interpret this mechanism to be related to conservation of angular momentum. The second is the classic Kelvin-Helmholtz mechanism, which is most sensitive to feedback involving the axial component of the perturbation momentum. This corresponds to the regions of strong shear around the bubble.

We have also considered the case of $Sw = 1.0$, which has two regions of absolute instability, one in the bubble and one in the wake. Our linear analysis has found that the region around the bubble is more influential than the wake in determining the growth rate and frequency. Previously, Gallaire *et al.* (2006) had found that the nonlinear frequency for this case is determined by the wake and our local analysis agrees with theirs. The frequencies from our analysis and Gallaire's analysis are both close to the limit-cycle frequency observed in Ruith *et al.*'s 3D DNS.

The sensitivity study of this paper provides useful information about the inherent dynamics of the flow. Knowing which regions are responsible for causing spiral vortex breakdown in swirling flows is the first step towards developing control strategies in such flows. From an engineering point of view, the approach used here can be extended,

following Marquet, Sipp & Jacquin (2008) and Meliga, Sipp & Chomaz (2010), to work out the sensitivity of the eigenvalue to a steady force acting on the swirling base flow. This will be more representative of the effect that a control device will have on the growth rate and frequency of the unstable mode and will be the subject of another paper.

Appendix. Equations in cylindrical co-ordinates, as used in code

This appendix contains the complex linearized direct and adjoint LMN equations that are solved to obtain the global modes.

A.1. *Linearized LMN equations representing equation 2.5*

A.1.1. *Momentum*

Axial:

$$
\begin{aligned}
(\sigma + \mathrm{i}\omega)\hat{m}_x \;=\; & -\frac{d\hat{p}}{dx} - \frac{\partial}{\partial x}\left(\hat{\rho}\bar{u}_x\bar{u}_x + 2\bar{\rho}\bar{u}_x\hat{u}_x\right)\ldots \\
& \ldots - \left(\frac{\partial}{\partial r} + \frac{1}{r}\right)\left(\bar{\rho}\bar{u}_r\hat{u}_x + \bar{\rho}\hat{u}_r\bar{u}_x + \hat{\rho}\bar{u}_x\bar{u}_r\right) \\
& \ldots - \frac{\mathrm{i}m}{r}\left(\bar{\rho}\bar{u}_\theta\hat{u}_x + \bar{\rho}\hat{u}_\theta\bar{u}_x + \hat{\rho}\bar{u}_x\bar{u}_\theta\right) + \frac{1}{S_1 Re}\left[\frac{\partial^2 \hat{u}_x}{\partial r^2} + \frac{1}{r}\frac{\partial \hat{u}_x}{\partial r} - \frac{m^2}{r^2}\hat{u}_x\ldots\right. \\
& \left. \ldots + \frac{1}{3}\left(4\frac{\partial^2 \hat{u}_x}{\partial x^2} + \frac{\partial^2 \hat{u}_r}{\partial x \partial r} + \frac{1}{r}\frac{\partial \hat{u}_r}{\partial x} + \frac{\mathrm{i}m}{r}\frac{\partial \hat{u}_\theta}{\partial x}\right)\right] \quad (\mathrm{A}\,1a)
\end{aligned}
$$

Radial:

$$
\begin{aligned}
(\sigma + \mathrm{i}\omega)\hat{m}_r \;=\; & -\frac{d\hat{p}}{dr} - \frac{\partial}{\partial x}\left(\bar{\rho}\bar{u}_r\hat{u}_x + \bar{\rho}\hat{u}_r\bar{u}_x + \hat{\rho}\bar{u}_x\bar{u}_r\right)\ldots \\
& \ldots - \left(\frac{\partial}{\partial r} + \frac{1}{r}\right)\left(\hat{\rho}\bar{u}_r\bar{u}_r + 2\bar{\rho}\bar{u}_r\hat{u}_r\right) - \frac{\mathrm{i}m}{r}\left(\bar{\rho}\bar{u}_\theta\hat{u}_r + \bar{\rho}\hat{u}_\theta\bar{u}_r + \hat{\rho}\bar{u}_r\bar{u}_\theta\right)\ldots \\
& \ldots - \frac{1}{r}\left(\hat{\rho}\bar{u}_\theta\bar{u}_\theta + 2\bar{\rho}\bar{u}_\theta\hat{u}_\theta\right) + \frac{1}{S_1 Re}\left[\frac{\partial^2 \hat{u}_r}{\partial x^2} - \frac{m^2}{r^2}\hat{u}_r\ldots\right. \\
& \left. \ldots + \frac{4}{3}\left(\frac{\partial^2 \hat{u}_r}{\partial r^2} + \frac{1}{r}\frac{\partial \hat{u}_r}{\partial r} - \frac{\hat{u}_r}{r^2}\right) + \frac{1}{3}\left(\frac{\partial^2 \hat{u}_x}{\partial x \partial r} + \frac{\mathrm{i}m}{r}\frac{\partial \hat{u}_\theta}{\partial r}\right) - \frac{7\mathrm{i}m}{3r^2}\hat{u}_\theta\right] \quad (\mathrm{A}\,2a)
\end{aligned}
$$

Azimuthal:

$$
\begin{aligned}
(\sigma + \mathrm{i}\omega)\hat{m}_\theta \;=\; & -\frac{\mathrm{i}m}{r}\hat{p} - \frac{\partial}{\partial x}\left(\bar{\rho}\bar{u}_\theta\hat{u}_x + \bar{\rho}\hat{u}_\theta\bar{u}_x + \hat{\rho}\bar{u}_x\bar{u}_\theta\right)\ldots \\
& \ldots - \left(\frac{\partial}{\partial r} + \frac{2}{r}\right)\left(\bar{\rho}\bar{u}_\theta\hat{u}_r + \bar{\rho}\hat{u}_\theta\bar{u}_r + \hat{\rho}\bar{u}_r\bar{u}_\theta\right)\ldots
\end{aligned}
$$

$$\ldots - \frac{\mathrm{i}m}{r}\left(\hat{\rho}\bar{u}_\theta\bar{u}_\theta + 2\bar{\rho}\bar{u}_\theta\hat{u}_\theta\right) + \frac{1}{S_1 Re}\left[\frac{\partial^2\hat{u}_\theta}{\partial x^2} + \frac{\partial^2\hat{u}_\theta}{\partial r^2} + \frac{1}{r}\frac{\partial\hat{u}_\theta}{\partial r}\ldots\right.$$

$$\left.\ldots - \left(1 + \frac{4m^2}{3}\right)\frac{\hat{u}_\theta}{r^2} + \frac{\mathrm{i}m}{3r}\left(\frac{\partial\hat{u}_x}{\partial x} + \frac{\partial\hat{u}_r}{\partial r}\right) - \frac{7\mathrm{i}m}{3r^2}\hat{u}_r\right] \qquad (A\,3a)$$

A.1.2. *Energy*

$$(\sigma + \mathrm{i}\omega)\hat{T} = -\frac{1}{\bar{\rho}}\left(\hat{m}_x\frac{\partial\bar{T}}{\partial x} + \hat{m}_r\frac{\partial\bar{T}}{\partial r}\right) - \bar{u}_x\frac{\partial\hat{T}}{\partial x} - \bar{u}_r\frac{\partial\hat{T}}{\partial r} - \frac{\mathrm{i}m\hat{u}_\theta}{r}\hat{T}\ldots$$

$$\ldots + \frac{1}{S_1 RePr\bar{\rho}}\left[\frac{\partial^2\hat{T}}{\partial x^2} + \frac{\partial^2\hat{T}}{\partial r^2} + \frac{1}{r}\frac{\partial\hat{T}}{\partial r} - \frac{m^2}{r^2}\hat{T}\right] \qquad (A\,4a)$$

A.1.3. *State*

$$\frac{\hat{\rho}}{\bar{\rho}^2} + (S_1 - 1)\hat{T} = 0 \qquad (A\,5)$$

A.2. *Adjoint LMN equations representing equation 2.9c*

A.2.1. *Momentum*

Axial:

$$(\sigma - \mathrm{i}\omega)\hat{m}_x^+ = \frac{1}{\bar{\rho}}\left(2\bar{m}_x\frac{\partial\hat{m}_x^+}{\partial x} + \bar{m}_r\left(\frac{\partial\hat{m}_r^+}{\partial x} + \frac{\partial\hat{m}_x^+}{\partial r}\right) + \bar{m}_\theta\left(\frac{\partial\hat{m}_\theta^+}{\partial x} + \frac{\mathrm{i}m}{r}\hat{m}_x^+\right)\right)\ldots$$

$$\ldots + \frac{1}{S_1 Re\bar{\rho}}\left[\frac{4}{3}\frac{\partial^2\hat{m}_x^+}{\partial x^2} + \frac{\partial^2\hat{m}_x^+}{\partial r^2} + \frac{1}{r}\frac{\partial\hat{m}_x^+}{\partial r} - \frac{m^2}{r^2}\hat{m}_x^+\ldots\right.$$

$$\left.\ldots + \frac{1}{3}\left(\frac{\partial^2\hat{m}_r^+}{\partial x\partial r} + \frac{1}{r}\frac{\partial\hat{m}_r^+}{\partial x} + \frac{\mathrm{i}m}{r}\frac{\partial\hat{m}_\theta}{\partial x}\right)\right] - \frac{\hat{T}^+}{\bar{\rho}}\frac{\partial\bar{T}}{\partial x} + \frac{1}{\bar{\rho}}\frac{\partial\hat{p}^+}{\partial x} \qquad (A\,6a)$$

Radial:

$$(\sigma - \mathrm{i}\omega)\hat{m}_r^+ = \frac{1}{\bar{\rho}}\left(\bar{m}_x\left(\frac{\partial\hat{m}_r^+}{\partial x} + \frac{\partial\hat{m}_x^+}{\partial r}\right) + 2\bar{m}_r\frac{\partial\hat{m}_r^+}{\partial r} + \bar{m}_\theta\left(\frac{\partial\hat{m}_\theta^+}{\partial r} + \frac{\mathrm{i}m}{r}\hat{m}_r^+ - \frac{\hat{m}_\theta^+}{r}\right)\right)\ldots$$

$$\ldots + \frac{1}{S_1 Re\bar{\rho}}\left[\frac{\partial^2\hat{m}_r^+}{\partial x^2} - \frac{m^2}{r^2}\hat{m}_r^+ + \frac{4}{3}\left(\frac{\partial^2\hat{m}_r^+}{\partial r^2} + \frac{1}{r}\frac{\partial\hat{m}_r^+}{\partial r} - \frac{\hat{m}_r^+}{r^2}\right)\ldots\right.$$

$$\left.\ldots + \frac{1}{3}\left(\frac{\partial^2\hat{m}_x^+}{\partial x\partial r} + \frac{\mathrm{i}m}{r}\frac{\partial\hat{m}_\theta^+}{\partial r}\right) - \frac{7\mathrm{i}m}{3r^2}\hat{m}_\theta^+\right] - \frac{\hat{T}^+}{\bar{\rho}}\frac{\partial\bar{T}}{\partial r} + \frac{1}{\bar{\rho}}\frac{\partial\hat{p}^+}{\partial r} \qquad (A\,7a)$$

Azimuthal:

$$(\sigma - \mathrm{i}\omega)\hat{m}_\theta^+ = \frac{1}{\bar{\rho}}\left(\bar{m}_x\left(\frac{\partial\hat{m}_\theta^+}{\partial x} + \frac{\mathrm{i}m}{r}\hat{m}_x^+\right) + \bar{m}_r\left(\frac{\partial\hat{m}_\theta^+}{\partial r} + \frac{\mathrm{i}m}{r}\hat{m}_r^+ - \frac{\hat{m}_\theta^+}{r}\right)\ldots\right.$$

$$\left.\ldots + \frac{2\bar{m}_\theta}{r}\left(\mathrm{i}m\hat{m}_\theta^+ + \hat{m}_r^+\right)\right) + \frac{1}{S_1 Re\bar{\rho}}\left[\frac{\partial^2\hat{m}_\theta^+}{\partial x^2} + \frac{\partial^2\hat{m}_\theta^+}{\partial r^2} + \frac{1}{r}\frac{\partial\hat{m}_\theta^+}{\partial r}\ldots\right.$$

$$\left.\ldots - \left(1 + \frac{4m^2}{3}\right)\frac{\hat{m}_\theta^+}{r^2} + \frac{\mathrm{i}m}{3r}\left(\frac{\partial\hat{m}_x^+}{\partial x} + \frac{\partial\hat{m}_r^+}{\partial r}\right) + \frac{7\mathrm{i}m}{3r^2}\hat{m}_r^+\right] + \frac{\mathrm{i}m}{r\bar{\rho}}\hat{p}^+ (A\,8a)$$

A.2.2. Energy

$$\hat{G}^+ = \frac{\hat{T}^+}{\bar{\rho}} + (S_1 - 1)\hat{p}^+ \tag{A 9a}$$

$$(\sigma - \mathrm{i}\omega)\hat{T}^+ = \bar{m}_x \frac{\partial \hat{G}^+}{\partial x} + \bar{m}_r \frac{\partial \hat{G}^+}{\partial r} + \frac{\mathrm{i}m}{r}\bar{m}_\theta \hat{G}^+ \dots$$

$$\dots + \frac{1}{S_1 RePr\bar{\rho}} \left[\frac{\partial^2 \hat{G}^+}{\partial x^2} + \frac{\partial^2 \hat{G}^+}{\partial r^2} + \frac{1}{r}\frac{\partial \hat{G}^+}{\partial r} - \frac{m^2}{r^2}\hat{G}^+ \right] \dots$$

$$\dots - (S_1 - 1)\hat{\rho}^+ \tag{A 9b}$$

A.2.3. State

$$\hat{\rho}^+ = -\bar{m}_x \left(\bar{m}_x \frac{\partial \hat{m}_x^+}{\partial x} + \bar{m}_r \frac{\partial \hat{m}_x^+}{\partial r} + \frac{\mathrm{i}m}{r}\bar{m}_\theta \hat{m}_x^+ \right) \dots$$

$$\dots - \bar{m}_r \left(\bar{m}_x \frac{\partial \hat{m}_r^+}{\partial x} + \bar{m}_r \frac{\partial \hat{m}_r^+}{\partial r} - \frac{1}{r}\bar{m}_\theta \hat{m}_\theta^+ + \frac{\mathrm{i}m}{r}\bar{m}_\theta \hat{m}_r^+ \right) \dots$$

$$\dots - \bar{m}_\theta \left(\bar{m}_x \frac{\partial \hat{m}_\theta^+}{\partial x} + \bar{m}_r \frac{\partial \hat{m}_\theta^+}{\partial r} + \frac{1}{r}\bar{m}_\theta \hat{m}_r^+ + \frac{\mathrm{i}m}{r}\bar{m}_\theta \hat{m}_\theta^+ \right) \dots$$

$$\dots - \frac{\bar{m}_x}{S_1 Re} \left[\frac{4}{3}\frac{\partial^2 \hat{m}_x^+}{\partial x^2} + \frac{\partial^2 \hat{m}_x^+}{\partial r^2} + \frac{1}{r}\frac{\partial \hat{m}_x^+}{\partial r} - \frac{m^2}{r^2}\hat{m}_x^+ \dots \right.$$

$$\dots + \frac{1}{3}\left(\frac{\partial^2 \hat{m}_r^+}{\partial x \partial r} + \frac{1}{r}\frac{\partial \hat{m}_r^+}{\partial x} + \frac{\mathrm{i}m}{r}\frac{\partial \hat{m}_\theta}{\partial x} \right) \Bigg] \dots$$

$$\dots - \frac{\bar{m}_r}{S_1 Re} \left[\frac{\partial^2 \hat{m}_r^+}{\partial x^2} - \frac{m^2}{r^2}\hat{m}_r^+ + \frac{4}{3}\left(\frac{\partial^2 \hat{m}_r^+}{\partial r^2} + \frac{1}{r}\frac{\partial \hat{m}_r^+}{\partial r} - \frac{\hat{m}_r^+}{r^2} \right) \dots \right.$$

$$\dots + \frac{1}{3}\left(\frac{\partial^2 \hat{m}_x^+}{\partial x \partial r} + \frac{\mathrm{i}m}{r}\frac{\partial \hat{m}_\theta^+}{\partial r} \right) - \frac{7\mathrm{i}m}{3r^2}\hat{m}_\theta^+ \Bigg] \dots$$

$$\dots - \frac{\bar{m}_\theta}{S_1 Re} \left[\frac{\partial^2 \hat{m}_\theta^+}{\partial x^2} + \frac{\partial^2 \hat{m}_\theta^+}{\partial r^2} + \frac{1}{r}\frac{\partial \hat{m}_\theta^+}{\partial r} \dots \right.$$

$$\dots - \left(1 + \frac{4m^2}{3} \right)\frac{\hat{m}_\theta^+}{r^2} + \frac{\mathrm{i}m}{3r}\left(\frac{\partial \hat{m}_x^+}{\partial x} + \frac{\partial \hat{m}_r^+}{\partial r} \right) + \frac{7\mathrm{i}m}{3r^2}\hat{m}_r^+ \Bigg] \tag{A 10a}$$

REFERENCES

BATCHELOR, G. K. 1967 *An introduction to fluid dynamics*. Cambridge University Press.

BENJAMIN, T. B. 1962 Theory of the vortex breakdown phenomenon. *Journal of Fluid Mechanics* **14** (4), 593 – 629.

CHANDLER, G. J., JUNIPER, M. P., NICHOLS, J. W. & SCHMID, P. J. 2012 Adjoint algorithms for the Navier-Stokes equations in the low Mach number limit. *Journal of Computational Physics* **231** (4), 1900–1916.

CHOMAZ, J.-M. 2005 Global instabilities in spatially developing flows: Non-normality and non-linearity. *Annual Review of Fluid Mechanics* **37**, 357–392.

CONSTANTINESCU, G. S. & LELE, S. K. 2002 A highly accurate technique for the treatment of flow equations at the polar axis in cylindrical coordinates using series expansions. *Journal of Computational Physics* **183** (1), 165–186.

ESCUDIER, M. 1988 Vortex breakdown: observations and explanations. *Progress in Aerospace Sciences* **25** (2).

GALLAIRE, F., RUITH, M., MEIBURG, E., CHOMAZ, J.-M. & HUERRE, P. 2006 Spiral vortex breakdown as a global mode. *Journal of Fluid Mechanics* **549**, 71–80.

GIANNETTI, F. & LUCHINI, P. 2007 Structural sensitivity of the first instability of the cylinder wake. *Journal of Fluid Mechanics* **581**, 167–197.

GRABOWSKI, W. J. & BERGER, S. A. 1976 Solutions of Navier-Stokes equations for vortex breakdown. *Journal of Fluid Mechanics* **75**, 525.

HALL, M. G. 1972 Vortex breakdown. *Annual Review of Fluid Mechanics* **4**, 195 –.

HEATON, C. J., NICHOLS, J. W. & SCHMID, P. J. 2009 Global linear stability of the non-parallel Batchelor vortex. *Journal of Fluid Mechanics* **629**, 139–160.

HILL, D. C. 1992 A theoretical approach for analyzing the re-stabilization of wakes. *AIAA Paper 92-0067* .

HUERRE, P. & MONKEWITZ, P. A. 1990 Local and global instabilities in spatially developing flows. *Annual Review of Fluid Mechanics* **22**, 473–537.

JUNIPER, M. P., TAMMISOLA, O. & LUNDELL, F. 2011 The local and global stability of confined planar wakes at intermediate Reynolds number. *Journal of Fluid Mechanics* **686**, 218–238.

LAMBOURNE, N. C. & BRYER, D. W. 1961 The bursting of leading-edge vortices- some observations and discussion of the phenomenon. Reports and Memoranda 3282. Aeronautical Research Council.

LEHOUCQ, R. B., SORENSEN, D. C. & YANG, C. 1998 ARPACK Users' Guide: Solution of Large-Scale Eigenvalue Problems with Implicity Restarted Arnoldi Methods. *SIAM* .

LEIBOVICH, S. 1978 Structure of vortex breakdown. *Annual Review of Fluid Mechanics* **10**, 221 – 246.

LEIBOVICH, S. & STEWARTSON, K. 1983 A sufficient condition for the instability of columnar vortices. *Journal of Fluid Mechanics* **126**, 335–356.

LUCCA-NEGRO, O. & O'DOHERTY, T. 2001 Vortex breakdown: a review. *Progress in Energy and Combustion Sciences* **27**, 431–481.

LUDWIEG, H. 1960 Stabilitat der Stromung in einem zylindrischen Ringraum. *Z. Flugwiss.* **8** (5), 135–140.

MARQUET, O., SIPP, D. & JACQUIN, L. 2008 Sensitivity analysis and passive control of cylinder flow. *Journal of Fluid Mechanics* **615**, 221–252.

MELIGA, P. & GALLAIRE, F. 2011 Global instability of helical vortex breakdown. 6th AIAA Theoretical Fluid Mechanics Conference, 27-30 June 2011, Honolulu, Hawaii.

MELIGA, P., GALLAIRE, F. & CHOMAZ, J.-M. 2012 A weakly nonlinear mechanism for mode selection in swirling jets. *Journal of Fluid Mechanics* .

MELIGA, P., SIPP, D. & CHOMAZ, J.-M. 2010 Open-loop control of compressible afterbody flows using adjoint methods. *Physics of Fluids* **22** (5).

NICHOLS, J. W., SCHMID, P. J. & RILEY, J. J. 2007 Self-sustained oscillations in variable-density round jets. *Journal of Fluid Mechanics* **582**, 341–376.

OBERLEITHNER, K., SIEBER, M., NAYERI, C. N., PASCHEREIT, C. O., PETZ, C., HEGE, H.-C., NOACK, B. R. & WYGNANSKI, I. 2011 Three-dimensional coherent structures in a swirling jet undergoing vortex breakdown: stability analysis and empirical mode construction. *Journal of Fluid Mechanics* .

PECKHAM, D. H. & ATKINSON, S. A. 1957 Preliminary results of low speed wind tunnel tests on a gothic wing of aspect ratio 1.0. *Tech. Rep..* Aeronautical Research Council.

PIER, B., HUERRE, P. & CHOMAZ, J.-M. 2001 Bifurcation to fully nonlinear synchronized structures in slowly varying media. *Physica D* **148**, 49–96.

RUITH, M. R., CHEN, P., MEIBURG, E. & MAXWORTHY, T. 2003 Three-dimensional vortex breakdown in swirling jets and wakes: direct numerical simulation. *Journal of Fluid Mechanics* **486**, 331–378.

SPALL, R. & SNYDER, D. 1999 Numerical simulations of vortex breakdown: Review and recent developments. *Recent Res. Developments on Heat, Mass and Momentum Transfer* **2**, 41–70.

TAMMISOLA, O. 2012 Oscillatory sensitivity patterns for global modes in wakes. *Journal of Fluid Mechanics* **701**, 251–277.

VYAZMINA, E., NICHOLS, J. W., CHOMAZ, J.-M. & SCHMID, P. J. 2009 The bifurcation structure of viscous steady axisymmetric vortex breakdown with open lateral boundaries. *Physics of Fluids* **21** (074107).